International Journal of Heat and Mass Transfer 55 (2012) 1291–1303

Contents lists available at SciVerse ScienceDirect

International Journal of Heat and Mass Transfer

journal homepage: www.elsevier.com/locate/ijhmt

Poiseuille flow of moderately rarefied gases in annular channels

Peyman Taheri [a,*], Henning Struchtrup [b]

[a] Mechatronic Systems Engineering, School of Engineering Science, Simon Fraser University, Surrey, British Columbia, Canada V3T 0A3
[b] Department of Mechanical Engineering, University of Victoria, P.O. Box 3055, STN CSC, Victoria, British Columbia, Canada V8W 3P6

ARTICLE INFO

Article history:
Received 24 February 2011
Received in revised form 9 July 2011
Available online 22 October 2011

Keywords:
Kinetic theory of gases
Rarefied gas flow
Poiseuille flow
Annular micro-channel
Knudsen boundary layer
Grad's moment method

ABSTRACT

In this study, rarefaction effects in pressure-driven gas flows in annular micro-channels are investigated. The influence of gas rarefaction, aspect ratio of the annulus, and surface accommodation coefficient on wall friction, mass flow rate, and thermal energy flow rate is studied. For this, the linearized Navier–Stokes–Fourier (NSF) and regularized 13-moment (R13) equations are solved analytically. The results are compared to available solutions of the Boltzmann equation to highlight the advantages of the R13 over the NSF equations in describing rarefaction effects in the process. Moreover, a second-order slip boundary condition is proposed to improve the accuracy of the classical NSF equations.

1. Introduction

Due to recent achievements in microfabrication, considerable interest in gas flows within miniaturized channels has emerged. Microchannels with different cross-sectional shapes are now widely used in a large variety of novel applications [1]. Examples are bipolar plates of microscale fuel cells, microstructured heat exchangers, microsensors and actuators, micro-nozzles, and biochemical lab-on-the-chip systems.

In gaseous flows, the measure for gas rarefaction is Knudsen number *Kn*, the ratio of the molecular mean free path and the geometric characteristic length of the flow. Accordingly, rarefied conditions are common in microsettings as well as in low-density (near vacuum) flows. Since in rarefied gas flows there are not sufficient collisions between the gas particles, an equilibrium state cannot be maintained, and nonequilibrium effects extend within the flow as the Knudsen number increases [2].

Precise microscopic solutions for rarefied gas flows, spanning the entire range of Knudsen number, require numerical solution of the Boltzmann kinetic equation [3,4]. Due to the complexity of the collision term in the Boltzmann equation, and the high dimensionality of the microscopic velocity field, kinetic solutions are computationally very expensive. Fortunately, when the Mach number is small and the flow is fully developed, which is the case for microflows, it suffices to solve the linearized Boltzmann equation which requires a considerably smaller computational effort [4].

It is well known that continuum fluid theories such as the Navier–Stokes and Fourier equations are valid only in the vicinity of equilibrium and fail to describe nonequilibrium effects in rarefied flows [5]. Instead, extended hydrodynamic equations, also referred to as "high-order macroscopic transport equations", which go beyond the classical Navier–Stokes–Fourier (NSF) system, are promising alternatives to kinetic approaches [5]. The Chapman–Enskog expansion [2] and Grad's moment expansion [6,7] are the classical methods to extract high-order macroscopic transport equations from the Boltzmann equation. Since these equations are deduced from the Boltzmann equation, they can describe rarefaction effects in dilute gas flows, yet with a considerably less computational cost. As a general rule, the size and complexity of extended hydrodynamic equations is proportional to the magnitude of the Knudsen number, since more moments (or equivalently, higher order of derivatives of macroscopic properties) are required to correctly describe the full spectrum of rarefaction effects. Hence, in highly rarefied situations their computational expense becomes comparable to that of the Boltzmann equation. For this reason, high-order macroscopic transport equations are recommended only for moderately rarefied flows, in particular for flows in the transition regime [8]. At the asymptotic limits of $Kn \to 0$ and $Kn \to \infty$ inexpensive equations can be used, i.e., the continuum NSF and collision less Boltzmann equations, respectively.

The regularized 13-moment (R13) equations [9] are the regularized version of the original Grad 13-moment (G13) equations [6]. They are based on moment approximations in kinetic gas theory,

* Corresponding author.
E-mail addresses: ptaherib@sfu.ca (P. Taheri), struchtr@uvic.ca (H. Struchtrup).
URL: http://www.sfu.ca/~ptaherib (P. Taheri).

0017-9310/$ - see front matter © 2011 Elsevier Ltd. All rights reserved.
doi:10.1016/j.ijheatmasstransfer.2011.09.012

Nomenclature

0	property at the reference equilibrium state
1	channel inlet
2	channel outlet
α	ratio of inner to outer radii
$\boldsymbol{\sigma}$	stress tensor [Pa]
χ	surface accommodation coefficient
Δr	circular gap size [m]
δ	rarefaction parameter
$\dot{E}$	thermal energy flow rate [kg m^2 s^{-3}]
$\dot{M}$	mass flow rate [kg s^{-1}]
ℓ	arbitrary macroscopic length [m]
Γ	perimeter [m]
κ	thermal conductivity coefficient [kg m^{-1} s^{-1}]
λ	molecular mean free path [m]
$\mathbf{I}$	unit tensor
$\mathbf{m}$	high-order moment tensor [N m^{-1} s^{-1}]
$\mathbf{q}$	heat flux vector [W]
$\mathbf{R}$	high-order moment tensor [N s^{-2}]
$\mathbf{v}$	velocity vector [m s^{-1}]
$\mathcal{C}$	normalized integrating constant
$\mathcal{R}$	gas constant [J kg^{-1} K^{-1}]
$\mathcal{V}$	slip velocity [m s^{-1}]
$\mathcal{F}$	thermodynamic force [kg s^{-1}]
A	model dependent coefficient
B	model dependent coefficient
C	integrating constant
μ	viscosity [kg m^{-1} s^{-1}]
ρ	density [kg m^{-3}]
$\sim$	dimensionless quantity
i	inner cylinder
o	outer cylinder
w	property at wall
θ	temperature in energy unit [J kg^{-1}]
$\widetilde{\mathcal{E}}$	dimensionless thermodynamic flux for thermal energy
$\widetilde{\mathcal{M}}$	dimensionless thermodynamic mass flux
φ	Azimuthal coordinate [Rad]
$\wp$	dimensionless pressure gradient
A	cross-sectional area [m^2]
D_h	hydraulic diameter [m]
f	Darcy friction factor
I_0	zeroth-order modified Bessel function of the first kind
Kn	Knudsen number
K_0	zeroth-order modified Bessel function of the second kind
L	channel length [m]
n	normal direction
p	pressure [Pa]
Po	Poiseuille number
Pr	Prandtl number
r	radial coordinate [m]
Re	Reynolds number
T	temperature [K]
t	tangential direction
u	mean velocity [m s^{-1}]
z	axial coordinate [m]
BGK	Bhatnagar–Gross–Krook model
G13	Grad 13-moment
LB	linearized Boltzmann model
NSF^1	Navier–Stokes–Fourier with first-order slip condition
NSF^2	Navier–Stokes–Fourier with second-order slip condition
R13	regularized 13-moment
T	transposed tensor

and are applicable to rarefied gas flows in the early transition regime, that is for Knudsen numbers up to 0.5, in some processes up to $Kn \approx 1$. The R13 system is the smallest set of moment equations which can properly describe Knudsen boundary layers [10–12]. In comparison to the G13 system, the R13 equations have shown superiority in describing shock structures [13], as well as nonequilibrium bulk effects [14,15]. Regularized moment equations with lower number of moments have been considered in Refs. [16,17], and equations with larger moment numbers have been studied in Refs. [12,18]. In general, more accurate but more expensive results can be obtained as the size of the moment system increases.

Burnett-type equations which are obtained as high-order systems from the Chapman–Enskog method suffer from linear instabilities [19], and lack a unified strategy to construct the required boundary conditions. Thus, they cannot be used as a simulation tool. On the other hand, moment equations, including the R13 equations, are stable [20], and they are furnished with boundary conditions for the moments [21,22]. These welcoming features allows the moment equations to be successfully adapted to many gas dynamic problems [18,23–25].

In the present work, the R13 equations are used to investigate nonequilibrium effects in Poiseuille flow of rarefied gases within channels of annular cross section. Isothermal slow flows, driven by small pressure gradients with relatively large Knudsen numbers $Kn \leqslant 1$, are computed from the linearized R13 equations, which are solved analytically. Due to the specific geometry of the flow passage, the analysis allows to investigate intermingling of rarefaction effects with curvature effects. For a similar geometry, shear-driven rotary flows were successfully simulated with the R13 equations [23].

To the authors' knowledge, linearized kinetic solutions for pressure-driven rarefied flows in annular channels are reported only in Refs. [26,27], and more recently in Ref. [28]. In [26,28] solutions of linearized Boltzmann equation with BGK model for the collision term is considered, while in [27] solutions of linearized Boltzmann equation with linear collision term is discussed. Furthermore, so far, this interesting problem has not been investigated through any extended macroscopic transport system. Here, theoretical solutions for shear stress, isothermal heat flow, velocity, and Knudsen boundary layers are presented, and their influence on mass transfer, heat transfer, and Poiseuille number is thoroughly demonstrated.

In the following, the linearized steady R13 equations and their boundary conditions are presented, and solved for the considered flow. In order to highlight advantage of the R13 equations over classical NSF equations, solutions of both systems are compared to some accurate kinetic data. Through comparisons it is shown that due to capability of the R13 equations in capturing of rarefaction effects, which are missing in NSF solutions, the R13 results match better with kinetic data. Our compact analytical solutions reveal that the presence of Knudsen boundary layers in the R13 solutions is the main reason for this improvement.

Various rarefaction effects such as Knudsen boundary layers (isothermal heat flow), slip velocity, and Knudsen paradox, which are captured in the R13 solutions with modest numerical effort, exhibit a good agreement to kinetic solutions. The presented results prove the usefulness of R13 system in predicting the mass and energy flow rates in rarefied situations, for Knudsen numbers up to unity. Even more, it is shown that furnishing the NSF equations with high-order boundary conditions improves the continuum results qualitatively; however, their inherent limitations do

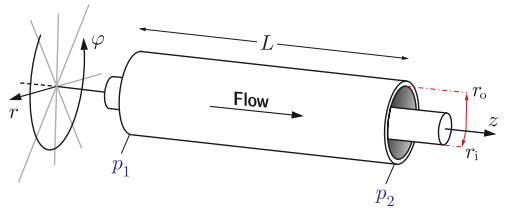

Fig. 1. Cylindrical coordinates and flow configuration in Poiseuille flow between two concentric cylinders with length L. The flow is driven by a constant pressure gradient in the axial direction. The inlet and outlet pressures are p_1 and p_2, and the annular gap size is $r_o - r_i$.

not allow to predict nongradient (rarefaction) transport phenomena within the Knudsen layers.

2. Formulation of the problem

The flow configuration is depicted in Fig. 1. An axial flow of a monatomic ideal gas, which is confined in the annulus between two stationary coaxial cylinders, is considered. Pressures at the inlet and outlet of the channel are p_1 and p_2, respectively, with $p_1 > p_2$. It is appropriate to use cylindrical coordinates $\mathbf{x} = \{r, \varphi, z\}$ where r and z are the radial and axial coordinates. The inner and outer radii of the circular gap are r_i and r_o, respectively, and the aspect ratio of the annulus is $\alpha = r_i/r_o$. The perimeter Γ, and the area A of the cross-section are

$$\Gamma = 2\pi(r_i + r_o) \quad \text{and} \quad A = \pi\left(r_o^2 - r_i^2\right), \tag{1}$$

and the hydraulic diameter D_h is defined as

$$D_h = 4\frac{A}{\Gamma} = 2\Delta r, \tag{2}$$

where $\Delta r = r_o - r_i$ is the gap size. The length of the flow passage, L, is assumed to be sufficiently large compared to its radial dimension, $L \gg \Delta r$, and thus boundary effects at entry and exit can be neglected. In the linear flow regime the flow temperature is constant and matches the temperature of the isothermal cylinders T^w. Here and below, the superscript 'w' refers to the properties at the cylindrical walls.

We investigate steady state flow of the gas, driven by a constant and small pressure gradient in z-direction. This constant pressure gradient can be treated as a body force applied along the channel. The flow is fully-developed, $\partial/\partial z = 0$, and the channel walls are impermeable; then there is no velocity in the radial direction, $v_r = 0$. Moreover, since the cylinders are stationary, the flow is irrotational, $v_\varphi = 0$, and independent of the azimuthal direction, i.e., $\partial/\partial\varphi = 0$.

We must emphasize that due to compressibility effects the actual flow in the annulus is two-dimensional in the r-z plane, which requires a numerical approach. However, for flows through long capillaries with small Mach numbers one can safely use linear analysis to discard the axial compressibility effects and simplify the problem such that a one-dimensional analysis suffices to investigate the local distribution of flow properties across the channel [29].

3. Regularized 13-moment equations

Monatomic ideal gases are considered where $p = \rho\mathcal{R}T = \rho\theta$ is the equation of state, in which p, ρ, and T are pressure, mass density, and thermodynamic temperature of the gas, respectively. For simplicity, the temperature in energy units $\theta = \mathcal{R}T$ is used, where $\mathcal{R} = k_B/m$ is the gas constant, with k_B and m as the Boltzmann constant and mass of the gas molecules, respectively.

The derivations of the fully nonlinear R13 equations and their corresponding boundary conditions in Cartesian coordinates are given in [9,22]. The nonlinear equations in cylindrical coordinates are presented in [25]; details on the transformation to cylindrical coordinates are available in Ref. [30].

For the present scenario we only need the linearized and steady-state equations. For linearization, we consider a reference state given by $p_0 = (p_1 + p_2)/2, \theta_0 = \mathcal{R}T^w$, and $\rho_0 = p_0/\theta_0 = (\rho_1 + \rho_2)/2$ in which the gas is at rest, $\mathbf{v}_0 = 0$, and in equilibrium, i.e., $\mathbf{q}_0 = \boldsymbol{\sigma}_0 = 0$. The vectors $\mathbf{v}$ and $\mathbf{q}$ correspond to velocity and heat flux, while $\boldsymbol{\sigma}$ is the stress deviator.

The core equations in the R13 system are the main conservation laws for mass, momentum, and energy densities, which in steady state and linearized form read

$$\nabla \cdot \mathbf{v} = 0, \tag{3}$$

$$\nabla \cdot \boldsymbol{\sigma} = -\nabla p, \tag{4}$$

$$\nabla \cdot \mathbf{q} = 0. \tag{5}$$

In the R13 system, stress deviator $\boldsymbol{\sigma}$ and heat-flux vector $\mathbf{q}$ are given by their respective moment equations [5,9,13,20] that again in steady state and linearized form are

$$\frac{4}{5}\langle\nabla\mathbf{q}\rangle + \nabla\cdot\mathbf{m} = -2p_0\langle\nabla\mathbf{v}\rangle - \frac{p_0}{\mu_0}\boldsymbol{\sigma}, \tag{6}$$

$$\theta_0\nabla\cdot\boldsymbol{\sigma} + \frac{1}{2}\nabla\cdot\mathbf{R} = -\frac{5}{2}p_0\nabla\theta - Pr\frac{p_0}{\mu_0}\mathbf{q}. \tag{7}$$

Here, μ_0 is the viscosity of the gas at the reference state, and Pr is the Prandtl number. In Eq. (7), we must set $\nabla\theta = 0$ for isothermal flows.

Closure for Eqs. (3)–(7) is obtained from regularization [9], and leads to constitutive relations for higher-order moments $\mathbf{R}$ and $\mathbf{m}$, which in linear form read

$$\mathbf{R} = -\mathsf{A}\frac{\mu_0}{\rho_0}\langle\nabla\mathbf{q}\rangle, \tag{8}$$

$$\mathbf{m} = -\mathsf{B}\frac{\mu_0}{\rho_0}\langle\nabla\boldsymbol{\sigma}\rangle. \tag{9}$$

In the equations above, terms inside angular brackets $\langle\cdots\rangle$ indicate the trace-free part of symmetric tensors. For instance, the trace-free part of the symmetric velocity gradient reads

$$\langle\nabla\mathbf{v}\rangle = \frac{1}{2}\left(\nabla\mathbf{v} + (\nabla\mathbf{v})^{\mathrm{T}}\right) - \frac{1}{3}\nabla\cdot\mathbf{v}\mathbf{I}, \tag{10}$$

where the superscript 'T' indicates the transposed tensor, and $\mathbf{I}$ is the unit tensor. For the trace-free part of rank-3 tensors see Appendix A in Ref. [5].

The Prandtl number in the moment equation for heat flux, and the coefficients A and B in the constitutive relations depend on the applied kinetic model [5]. For the Bhatnagar–Gross–Krook (BGK) kinetic model these coefficients are

$$Pr^{\mathrm{BGK}} = 1, \quad \mathsf{A}^{\mathrm{BGK}} = \frac{28}{5}, \quad \mathsf{B}^{\mathrm{BGK}} = 3, \tag{11a}$$

and for the linearized Boltzmann (LB) kinetic model they read

$$Pr^{\mathrm{LB}} = \frac{2}{3}, \quad \mathsf{A}^{\mathrm{LB}} = \frac{24}{5}, \quad \mathsf{B}^{\mathrm{LB}} = 2. \tag{11b}$$

In the hydrodynamics limit where the high-order moments $\mathbf{R}$ and $\mathbf{m}$ vanish, the terms on the left-hand side of Eqs. (6) and (7) are zero. Therefore, Eqs. (6) and (7) reduce to the linearized Navier–Stokes and Fourier laws of classical hydrodynamics, i.e., Newtonian viscous shear and Fourier's heat conduction,

$$\boldsymbol{\sigma} = -2\mu_0\langle\nabla\mathbf{v}\rangle, \tag{12}$$

$$\mathbf{q} = -\kappa\nabla\theta, \tag{13}$$

where $\kappa = 5\mu_0/(2Pr)$ is the thermal conductivity coefficient for ideal gases. In isothermal flows, Fourier's heat flux (13) vanishes, since $\nabla\theta = 0$. Eqs. (12) and (13) along with the conservation laws (3)–(5) form the linearized Navier–Stokes–Fourier system,

$$\nabla\cdot\mathbf{v} = 0, \quad \mu_0\nabla^2\mathbf{v} = \nabla p, \quad \nabla^2\theta = 0. \tag{14}$$

4. Wall boundary conditions

Boundary conditions are necessary to find a unique solution for the considered boundary value problem. Wall boundary conditions express the properties of the gas adjacent to the wall with respect to the wall temperature and the wall velocity. Detailed discussion on wall boundary conditions for R13 equations is available in Refs. [22,30], where macroscopic boundary conditions for high-order moments are derived from Maxwell's boundary condition for the Boltzmann equation [31].

4.1. Boundary conditions for the R13 equations

For isothermal flows the required boundary conditions in linearized form are [22,30]

$$\sigma_{tn} = \frac{\chi}{2-\chi}\sqrt{\frac{2}{\pi\theta_0}}\left(-p_0\mathcal{V}_t - \frac{1}{5}q_t - \frac{1}{2}m_{tnn}\right), \tag{15a}$$

$$R_{tn} = \frac{\chi}{2-\chi}\sqrt{\frac{2}{\pi\theta_0}}\left(p_0\theta_0\mathcal{V}_t - \frac{11}{5}\theta_0 q_t - \frac{1}{2}\theta_0 m_{tnn}\right), \tag{15b}$$

where the subscripts 't' and 'n' indicate *tangential* and *normal* directions with respect to the wall, respectively, that is the z- and r-directions [cf. Fig. 1]. The wall normal points in the radial direction toward the gas, thus, wall normal vectors have opposite signs on the inner and outer cylinders. $\mathcal{V}_t = v_t - v_t^{\mathrm{w}}$ is slip velocity on the wall. Effects of gas-surface interaction are reflected in the surface accommodation coefficient χ, where $\chi = 0$ and $\chi = 1$ describe fully reflective (smooth) and fully diffusive (rough) walls, respectively.

In the linear setting, temperature and velocity problems decouple [11,14]. Since for the present study we are interested in isothermal flows, the velocity problem is solved only. Eqs. (15) are the boundary conditions for the velocity problem. Additional boundary conditions are required when flow is non-isothermal [22].

4.2. Second-order slip condition for NSF equations

When evaluated by means of the Chapman–Enskog expansion method [2], the R13 boundary conditions in Eq. (15) include first- and second-order moments [15]. Scaling of the second-order moments leads to second-order velocity slip and temperature jump boundary conditions for the Navier–Stokes–Fourier system. Here, since isothermal flows are considered, only the velocity slip condition is required, which in linear form reads [25,30]

$$\mathcal{V}_z^{\mathrm{NSF}} = -\frac{2-\chi}{\chi}\sqrt{\frac{\pi\theta_0}{2}}\frac{\sigma_{rz}^{\mathrm{NSF}}}{p_0}n_r + \left[\left(\frac{1}{5Pr}+\frac{4\mathrm{B}}{15}\right)\frac{\partial\sigma_{rz}^{\mathrm{NSF}}}{\partial r} + \left(\frac{1}{5Pr}-\frac{\mathrm{B}}{15}\right)\frac{\sigma_{rz}^{\mathrm{NSF}}}{r}\right]\frac{\mu_0\theta_0}{p_0^2}. \tag{16}$$

The quantity $\sigma_{rz}^{\mathrm{NSF}}$ denotes the Navier–Stokes shear stress, Eq. (12). The first term represents the first-order slip velocity, and the others are second-order corrections. The term $\sigma_{rz}^{\mathrm{NSF}}/r$ is a curvature effect of the channel walls on the slip velocity. The wall normal is indicated by n_r, with $n_r = +1$ for the inner wall and $n_r = -1$ for the outer wall.

5. Flow equations

In order to investigate Poiseuille flow in annular channels, the R13 Eqs. (3)–(9) and the NSF Eq. (14) are transformed into cylindrical coordinates.

For the considered flow configuration, as discussed in Section 2, the velocity vector $\mathbf{v}$, the heat-flux vector $\mathbf{q}$, and stress tensor $\boldsymbol{\sigma}$ simplify to

$$\mathbf{v} = \begin{pmatrix} 0 \\ 0 \\ v_z(r) \end{pmatrix}, \quad \mathbf{q} = \begin{pmatrix} q_r(r) \\ 0 \\ q_z(r) \end{pmatrix}, \quad \boldsymbol{\sigma} = \begin{pmatrix} \sigma_{rr}(r) & 0 & \sigma_{rz}(r) \\ 0 & \sigma_{\varphi\varphi}(r) & 0 \\ \sigma_{rz}(r) & 0 & \sigma_{zz}(r) \end{pmatrix}, \tag{17}$$

where all components only depend on the radial coordinate r. Since the stress tensor is trace free, we have $\sigma_{\varphi\varphi}(r) = -\sigma_{rr}(r) - \sigma_{zz}(r)$.

In order to present a general analysis, it is useful to proceed with dimensionless equations. The reference state properties $\{p_0, \rho_0, \theta_0\}$ and a macroscopic length scale ℓ can be used to define dimensionless quantities. The radial coordinate, axial coordinate, perimeter, and area are normalized with respect to the macroscopic length scale,

$$\tilde{r} = \frac{r}{\ell}, \quad \tilde{z} = \frac{z}{\ell}, \quad \tilde{\Gamma} = \frac{\Gamma}{\ell}, \quad \tilde{A} = \frac{A}{\ell^2}. \tag{18a}$$

The remaining variables in dimensionless form are defined as

$$\tilde{\rho} = \frac{\rho}{\rho_0}, \quad \tilde{\theta} = \frac{\theta}{\theta_0}, \quad \tilde{p} = \frac{p}{p_0}, \quad \tilde{\mathbf{v}} = \frac{\mathbf{v}}{\sqrt{\theta_0}}, \quad \tilde{\mathbf{q}} = \frac{\mathbf{q}}{p_0\sqrt{\theta_0}}, \quad \tilde{\boldsymbol{\sigma}} = \frac{\boldsymbol{\sigma}}{p_0}, \quad \tilde{\mathbf{R}} = \frac{\mathbf{R}}{p_0\theta_0}, \quad \tilde{\mathbf{m}} = \frac{\mathbf{m}}{p_0\sqrt{\theta_0}}, \tag{18b}$$

where the isothermal speed of sound $\sqrt{\theta_0}$ is employed as the velocity scale. The tilde signs indicate dimensionless quantities. Furthermore, $\tilde{\mu} = \mu/\mu_0$ is the dimensionless viscosity with $\mu_0 = \mu(\theta_0)$. In ideal gases viscosity is a function of temperature only [5], hence, in our analysis, due to the assumption of isothermal flow, the dimensionless viscosity turns to be a constant, $\tilde{\mu} = 1$. In our treatment of nonisothermal flow problems, in order to achieve an analytical solution, dependency of viscosity on temperature was neglected [24,25]. A more refined approach would include this temperature dependence, similar to [32].

After applying differential operators in cylindrical geometry [30], and using the above dimensionless quantities, Eqs. (3)–(9) cast into the dimensionless form of the linearized R13 equations in cylindrical coordinates,

$$\left(\frac{\partial}{\partial\tilde{r}} + \frac{1}{\tilde{r}}\right)\tilde{\sigma}_{rz} = -\wp, \tag{19a}$$

$$-\wp + \frac{1}{2}\left(\frac{\partial}{\partial\tilde{r}} + \frac{1}{\tilde{r}}\right)\tilde{R}_{rz} = -\frac{Pr}{Kn}\tilde{q}_z, \tag{19b}$$

$$\frac{2}{5}\frac{\partial\tilde{q}_z}{\partial\tilde{r}} + \left(\frac{\partial}{\partial\tilde{r}} + \frac{1}{\tilde{r}}\right)\tilde{m}_{rrz} - \frac{\tilde{m}_{\varphi\varphi z}}{\tilde{r}} = -\frac{\partial\tilde{v}_z}{\partial\tilde{r}} - \frac{1}{Kn}\tilde{\sigma}_{rz}, \tag{19c}$$

where $\wp$ is the dimensionless pressure gradient along the axial direction (a negative quantity for the flow setting in Fig. 1)

$$\wp = \frac{\ell}{p_0}\frac{\partial p}{\partial z} = \frac{\partial\tilde{p}}{\partial\tilde{z}}. \tag{20}$$

In the dimensionless equations the reference viscosity coefficient μ_0 gives rise to the mean free path λ_0 in the gas at the reference state. Accordingly, the Knudsen number

$$Kn = \frac{\lambda_0}{\ell} \quad \text{with} \quad \lambda_0 = \frac{\mu_0\sqrt{\theta_0}}{p_0}, \tag{21}$$

appears in the dimensionless equations. The Knudsen number is the measure for gas rarefaction.

Eqs. (19a) and (19b) are the linearized and dimensionless momentum balance (Eq. (4)) and heat-flux balance (Eq. (7)) in z-direction. The dimensionless form of the linearized shear-stress balance is given in Eq. (19c). The relevant dimensionless high-order moments in (19) follow from Eqs. (8) and (9) as

$$\tilde{R}_{rz} = -\frac{1}{2}\mathrm{A}\,Kn\frac{\partial \tilde{q}_z}{\partial \tilde{r}}, \tag{22a}$$

$$\tilde{m}_{rrz} = \frac{8}{15}\mathrm{B}\,Kn\left(\wp + \frac{5}{4}\frac{\tilde{\sigma}_{rz}}{\tilde{r}}\right), \tag{22b}$$

$$\tilde{m}_{\varphi\varphi z} = -\frac{2}{15}\mathrm{B}\,Kn\left(\wp + 5\frac{\tilde{\sigma}_{rz}}{\tilde{r}}\right). \tag{22c}$$

The required boundary conditions for the problem are the same as in (15), that in dimensionless form and with proper coordinate-indicative indices read

$$\tilde{\sigma}_{rz} = \frac{\chi}{2-\chi}\sqrt{\frac{2}{\pi}}\left(-\tilde{v}_z - \frac{1}{5}\tilde{q}_z - \frac{1}{2}\tilde{m}_{rrz}\right)n_r, \tag{23a}$$

$$\tilde{R}_{rz} = \frac{\chi}{2-\chi}\sqrt{\frac{2}{\pi}}\left(\tilde{v}_z - \frac{11}{5}\tilde{q}_z - \frac{1}{2}\tilde{m}_{rrz}\right)n_r. \tag{23b}$$

As mentioned in Section 3, in the asymptotic limit of $Kn \to 0$ the R13 equations reduce to the NSF equations, i.e., the system (19) reduces to

$$\left(\frac{\partial}{\partial \tilde{r}} + \frac{1}{\tilde{r}}\right)\frac{\partial \tilde{v}_z}{\partial \tilde{r}} = \frac{\wp}{Kn}, \tag{24a}$$

$$\frac{\partial \tilde{\theta}}{\partial \tilde{z}} = 0. \tag{24b}$$

The above results from substituting the linearized Navier–Stokes and Fourier laws (Eqs. (12) and (13)) in dimensionless form, which read

$$\tilde{\sigma}_{rz}^{\mathrm{NSF}} = -Kn\frac{\partial \tilde{v}_z}{\partial \tilde{r}}, \quad \tilde{q}_z^{\mathrm{NSF}} = -\frac{5}{2}\frac{Kn}{Pr}\frac{\partial \tilde{\theta}}{\partial \tilde{z}}. \tag{25}$$

It follows from Eq. (19a), that the pressure gradient $\wp$ is of first-order in terms of Knudsen number, $\mathcal{O}(\wp) = \mathcal{O}(Kn)$. Hence, $\wp$ in Eq. (19b) provides a second-order contribution to the axial heat flux, which vanishes in the hydrodynamic limit [4], that is it does not appear in Eq. (24b).

The dimensionless slip condition (16) for NSF is

$$\tilde{v}_z^{\mathrm{NSF}} = -\frac{2-\chi}{\chi}\sqrt{\frac{\pi}{2}}\tilde{\sigma}_{rz}^{\mathrm{NSF}}n_r + \left[\left(\frac{1}{5Pr} + \frac{4\mathrm{B}}{15}\right)\frac{\partial \tilde{\sigma}_{rz}^{\mathrm{NSF}}}{\partial \tilde{r}} + \left(\frac{1}{5Pr} - \frac{\mathrm{B}}{15}\right)\frac{\tilde{\sigma}_{rz}^{\mathrm{NSF}}}{\tilde{r}}\right]Kn. \tag{26}$$

As given in Eq. (25), since $\mathcal{O}(\tilde{\sigma}_{rz}) = \mathcal{O}(Kn)$, the first and second terms in (26) respectively contribute to the first- and second-order slip corrections.

6. Results and discussion

6.1. Analytical solutions for R13 equations

Replacement of (22) into (19) and subsequent integration gives the following analytical solutions for shear stress $\tilde{\sigma}_{rz}$, streamwise heat flux $\tilde{q}_z$, and velocity $\tilde{v}_z$,

$$\tilde{\sigma}_{rz} = \underline{-\frac{\wp}{2}\tilde{r} + \frac{\mathrm{C}_1}{\tilde{r}}}, \tag{27a}$$

$$\tilde{q}_z = \mathrm{C}_2 I_0\left(\frac{2}{Kn}\sqrt{\frac{Pr}{\mathrm{A}}}\tilde{r}\right) + \mathrm{C}_3 K_0\left(\frac{2}{Kn}\sqrt{\frac{Pr}{\mathrm{A}}}\tilde{r}\right) + \frac{Kn\wp}{Pr}, \tag{27b}$$

$$\tilde{v}_z = \underline{\mathrm{C}_4 + \frac{\wp}{4Kn}\tilde{r}^2 - \frac{\mathrm{C}_1}{Kn}\ln(\tilde{r})} - \frac{2}{5}\tilde{q}_z. \tag{27c}$$

In the above general solutions C_1 to C_4 are the integrating constants, which must be determined from the boundary conditions on both inner and outer walls. The constants were computed using the analytical software package Mathematica®, which was also used to generate the plots shown below. In the NSF solutions, the constants in an abstract form read,

$$\mathrm{C}_1^{\mathrm{NSF}^1} = \wp\mathcal{C}_1^{\mathrm{NSF}^1}(\alpha, \chi, Kn), \quad \mathrm{C}_4^{\mathrm{NSF}^1} = \wp\mathcal{C}_4^{\mathrm{NSF}^1}(\alpha, \chi, Kn), \tag{28a}$$

$$\mathrm{C}_1^{\mathrm{NSF}^2} = \wp\mathcal{C}_1^{\mathrm{NSF}^2}(\alpha, \chi, \mathrm{B}, Kn), \quad \mathrm{C}_4^{\mathrm{NSF}^2} = \wp\mathcal{C}_4^{\mathrm{NSF}^2}(\alpha, \chi, \mathrm{B}, Kn, Pr), \tag{28b}$$

while $\mathrm{C}_2^{\mathrm{NSF}^{1,2}} = \mathrm{C}_3^{\mathrm{NSF}^{1,2}} = 0$. In the R13 solutions, all the integrating constants take the following form,

$$\mathrm{C}_i^{\mathrm{R13}} = \wp\mathcal{C}_i^{\mathrm{R13}}(\alpha, \chi, \mathrm{A}, \mathrm{B}, Kn, Pr). \tag{28c}$$

It can be seen that all of the integrating constants in NSF and R13 are linear function of pressure gradient $\wp$. Due to bulky expressions for $\mathcal{C}_1$ to $\mathcal{C}_4$, we have not explicitly shown these functions.

The underlined terms indicate the solution of the NSF equations. Note that the general solution for shear stress is identical for both R13 and NSF systems. Since NSF yields heat flow only in presence of a temperature gradient, it cannot predict the axial heat flux $\tilde{q}_z$ in this isothermal flow. This streamwise heat flow, which is not driven by a temperature gradient, is a pure rarefaction effect. The zeroth-order modified Bessel functions I_0 and K_0 in the heat-flux solution represent the Knudsen boundary layers, while $Kn\wp/Pr$ is a high-order bulk effect. The R13 velocity solution shows that isothermal heat flux contributes in the flow velocity. This effect is missing in the NSF velocity solution. The values of $\tilde{v}_z$ at $\tilde{r}_\mathrm{i}$ and $\tilde{r}_\mathrm{o}$ are the slip velocities.

For $\chi = 1$, $\alpha = 0.1$, and $Kn = \{0.02, 0.2\}$ the solutions (27) are plotted in Fig. 2, which are normalized with respect to the pressure gradient–note that all the integrating constants linearly depend on $\wp$. The NSF results with first-order slip condition (NSF^1) and second-order slip condition (NSF^2) are compared to the R13 results.

The general solution for shear-stress (Eq. (27a)) is the same for NSF and R13, but their specific solutions differ due to different values for the integrating constant (C_1 is different for NSF and R13), which are obtained from different boundary conditions. As shown in plot (a), in weakly rarefied flows ($Kn = 0.02$) the shear stress profiles for NSF and R13 are very close. For the larger Knudsen number $Kn = 0.2$ [cf. plot (b)] NSF^1 is considerably different from R13 (specifically on the inner cylinder), while NSF^2 and R13 are in complete agreement. This shows that application of second-order slip condition corrects the NSF shear-stress solution to match with the R13 solution.

For $Kn = 0.02$, BGK and LB results coincide. As the Knudsen number increases, the solutions with BGK coefficients yield slightly higher shear stress on the inner wall, compared to LB coefficients. Unfortunately, kinetic data (i.e., solutions of the Boltzmann equation) for shear stress is not reported in the literature. The validity of our shear-stress solutions is discussed in Section 6.2.1, where the Poiseuille number is evaluated from the NSF and R13 solutions and compared to kinetic data.

According to Fourier's law, heat flow in the NSF theory is the result of a temperature gradient. Therefore, in the considered isothermal flow, NSF fails to predict the axial heat flow, $\tilde{q}_z^{\mathrm{NSF}} = 0$. In plots (c) and (d) of Fig. 2, the NSF and R13 solutions for axial heat flow (Eq. (27b)) are plotted. For $Kn = 0.02$, the constant bulk heat

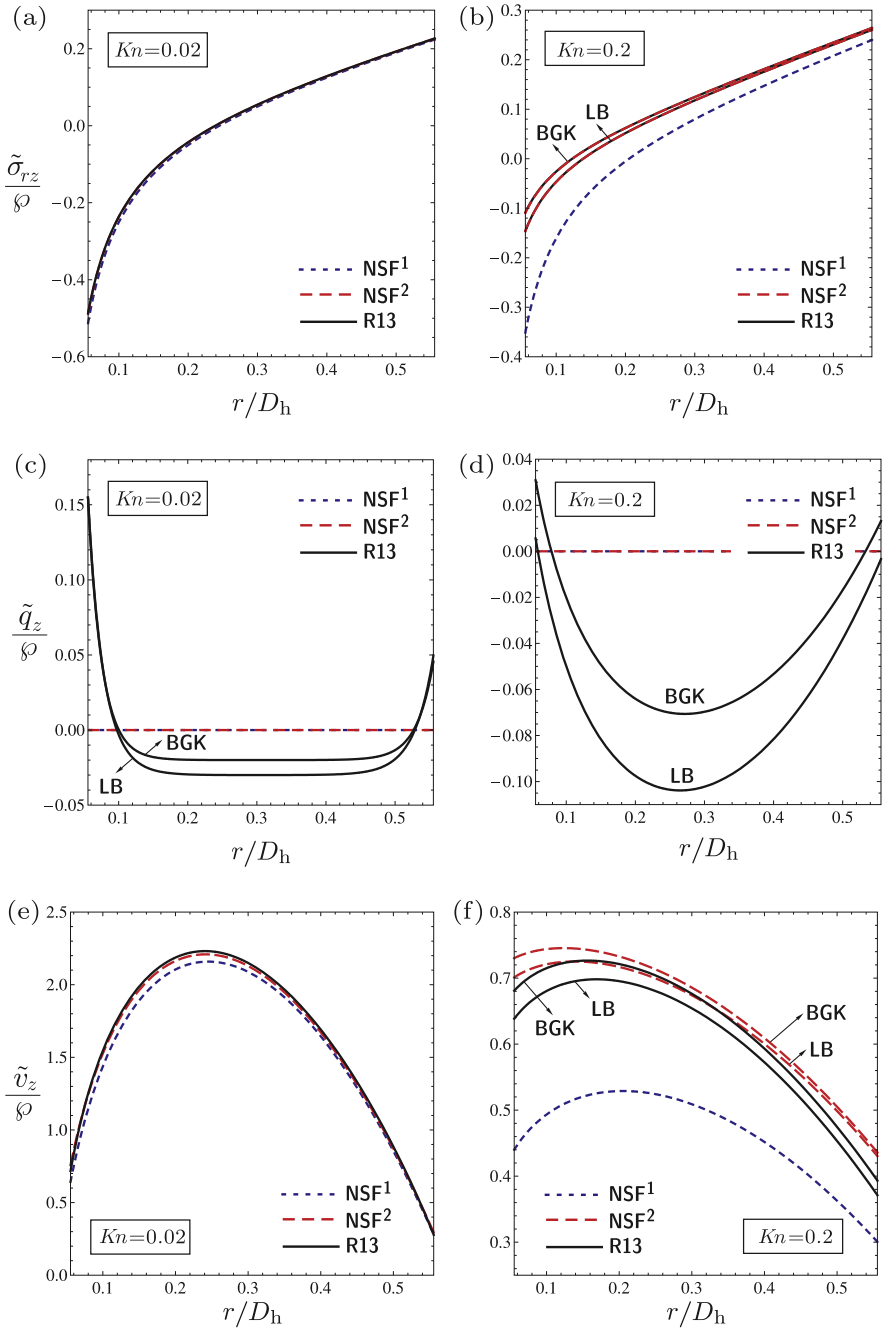

Fig. 2. Normalized distribution of shear stress, isothermal heat flux, and velocity across the annulus are plotted. The plots are obtained for $\chi = 1$, $\alpha = 0.1$, with both BGK and LB coefficients. Solutions for NSF with first-order slip condition (NSF[1]), and second-order slip condition (NSF[2]) are compared to R13 results for $Kn = 0.02$ (left plots), and $Kn = 0.2$ (right plots). We emphasize that the difference between shear-stress solutions for NSF and R13 is rooted in evaluation of the integrating constant C_1.

flow is dominant in the center of the channel. The bulk heat flow occurs in the opposite direction of mass flow. Thin Knudsen boundary layers are visible close to the walls. For $Kn = 0.2$, the thickness of the Knudsen layers is increased such that the whole channel is affected by nonequilibrium boundary effects.

The differences between BGK and LB solutions for heat flow are rooted in their coefficients (11). In general, the bulk heat flow in the LB model is 50% stronger than for the BGK model. Unfortunately, kinetic data for the isothermal heat flux are not available for comparison. The validity of our heat-flux solutions are discussed in Section 6.2.2, where the thermal energy flow rate is evaluated from NSF and R13 solutions and compared to kinetic data.

Plots (e) and (f) of Fig. 2 show the velocity profiles. For small Knudsen number $Kn = 0.02$, the NSF and R13 solutions are in fair agreement. Moreover, application of the BGK and LB coefficients leads to a negligible dissimilarity. Differences appear at the larger Knudsen number $Kn = 0.2$, where NSF[1] drastically underpredicts the velocity. It is evident that application of second-order slip condition (26) shifts the NSF solution closer to the R13 results. The difference between the NSF[2] and R13 solutions is due to the boundary conditions and the absence of Knudsen boundary layers from the NSF solution (27c).

To demonstrate how the R13 velocity distribution depends on nonequilibrium effects, in Fig. 3, full R13 velocity solution is compared to the cases in which Knudsen layers and the high-order bulk term ($Kn_\wp/Pr$) are neglected. These plots are obtained for $\chi = 1$, $\alpha = 0.1$, $Kn = \{0.1, 0.2\}$, and LB coefficients (11b). As shown in the plots, neglection of the Knudsen layers leads to velocity

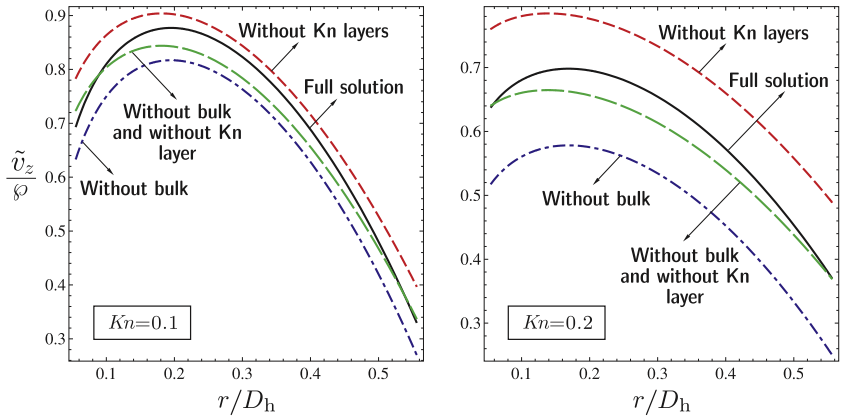

Fig. 3. Dependency of the R13 velocity solution to nonequilibrium effects is demonstrated for $\chi = 1$, $\alpha = 0.1$, and $Kn = \{0.1, 0.2\}$.

overprediction, since less friction is evaluated on the boundaries. On the other hand, the absence of the bulk term gives a lower velocity results. Combination of the high-order bulk term and Knudsen layers, as given by Eq. (27c), yields the R13 velocity profile.

Variation of normalized integrating constants with respect to Knudsen number for $\chi = 1$ and $\alpha = 0.1$ are plotted in Fig. 4. The plots are obtained for LB coefficients (11b). The constant $\mathcal{C}_1$ for NSF[2] and R13 is the same, which leads to identical stress solutions for these systems.

To show the influence of the annulus aspect ratio $\alpha = r_i/r_o$ on velocity distribution, normalized velocity solutions are plotted in Fig. 5 for $\chi = 1$, $Kn = 0.1$, and $\alpha = \{0.1, 0.9\}$. For the plots the BGK coefficients in Eq. (11a) are employed. For $\alpha = 0.1$, the curvature difference between the inner and outer walls is large, and the velocity profiles are asymmetric with respect to the centerline of the annulus. The curvature effects diminish when the size of the gap decreases (α increases). As shown, for $\alpha = 0.9$ the velocity distribution is almost symmetric, similar to planar Poiseuille flow [14]. The same behaviour was observed for $\tilde{\sigma}_{rz}$ and $\tilde{q}_z$ when $\alpha \to 1$ (not shown).

Explicit kinetic data for velocity are not available. The validity of our velocity solutions is discussed in Section 6.2.2, where the mass flow rate is evaluated from NSF and R13 solutions and compared to kinetic data.

6.2. Comparison with kinetic data

Comparison of our theoretical results with kinetic solutions of the Boltzmann equation are presented in this section. For the considered problem kinetic data for both the linearized Boltzmann (LB) equation and the Bhatnagar–Gross–Krook (BGK) equation

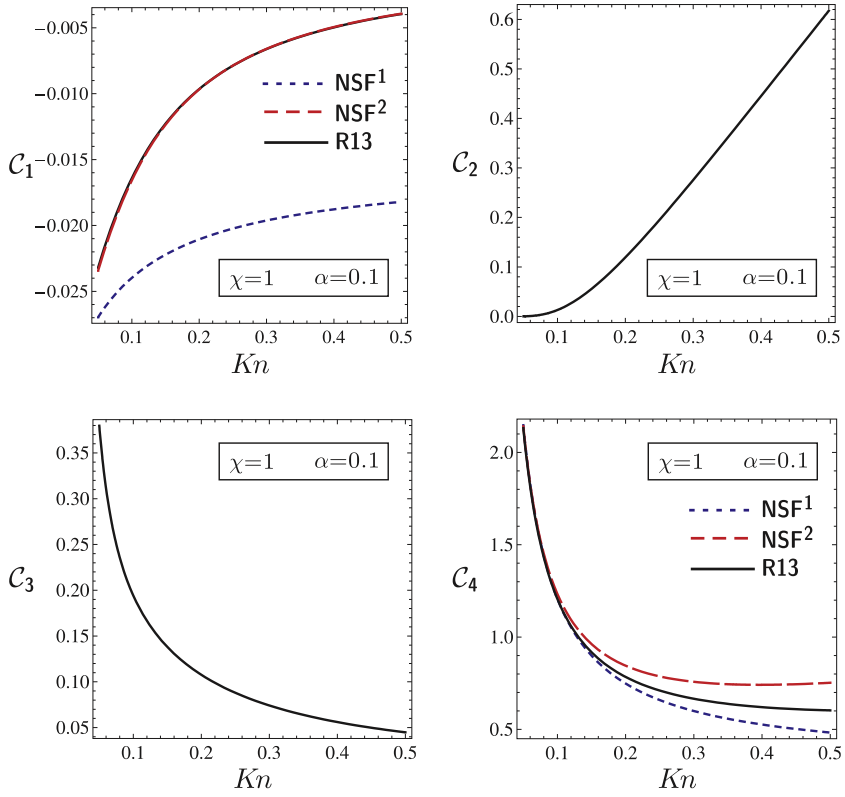

Fig. 4. For $\chi = 1$ and $\alpha = 0.1$, normalized integrating constants $\mathcal{C}_1$ to $\mathcal{C}_4$, are plotted with respect to Knudsen number.

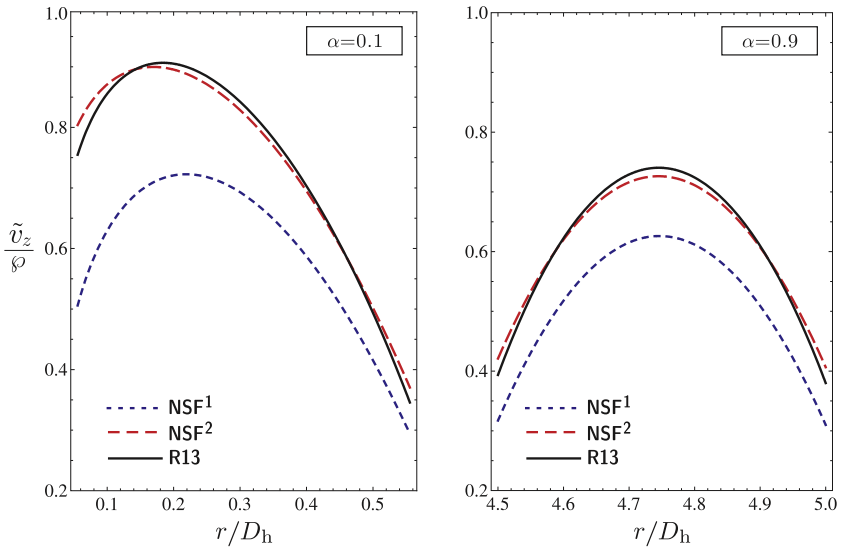

Fig. 5. Dependency of velocity distribution on α (the ratio of inner to outer cylinder) is demonstrated for $\chi = 1$, $Kn = 0.1$, and BGK coefficients.

are reported in [27,28]. In order to compare our solutions with the results of each kinetic equation, the proper coefficients must be used in the R13 model, see Eq. (11).

In the kinetic approaches [27,28] the rarefaction parameter δ is defined as

$$\delta = \frac{p_0 \ell}{\mu_0 \sqrt{2\theta_0}} = \frac{1}{\sqrt{2} Kn}, \tag{29}$$

where its relation to our definition of the Knudsen number follows from Eqs. (21) and (29).

In contrast to discrete kinetic solutions, our analytical solutions (27) are continuous, hence, they are preferred for parametric studies. Moreover, the computational time for the presented approach is considerably less than kinetic approaches. For instance, on a single core ×86–64 CPU, BGK simulations take minutes to hours as δ increases [28], while with the same CPU our simulation takes a fraction of a minute.

6.2.1. Poiseuille number

In the axial momentum balance (Eq. (19a)), the divergence of shear stress and the gradient of pressure describe the momentum flux in axial direction. Since the pressure gradient is constant, integration of this equation over the cross section gives

$$\Gamma \sigma^{\mathrm{w}} = A \frac{\partial p}{\partial z} \quad \text{or} \quad \frac{\tilde{\sigma}^{\mathrm{w}}}{\wp} = \frac{A}{\ell \Gamma}, \tag{30}$$

where $\sigma^{\mathrm{w}} = p_0 \tilde{\sigma}^{\mathrm{w}}$ is the mean shear stress on the walls,

$$\tilde{\sigma}^{\mathrm{w}} = \frac{\tilde{r}_{\mathrm{i}} \tilde{\sigma}_{rz}(\tilde{r}_{\mathrm{i}}) + \tilde{r}_{\mathrm{o}} \tilde{\sigma}_{rz}(\tilde{r}_{\mathrm{o}})}{\tilde{r}_{\mathrm{i}} + \tilde{r}_{\mathrm{o}}}. \tag{31}$$

Setting $\ell = D_{\mathrm{h}}$ in Eq. (30) and using Eq. (2) gives

$$\frac{\tilde{\sigma}^{\mathrm{w}}}{\wp} = \frac{1}{4}, \tag{32}$$

which holds for all values of the coefficients Kn, α, and χ.

The Poiseuille number Po, is defined as the product of the Darcy friction factor f, and the Reynolds number based on the hydraulic diameter, $Re_{D_{\mathrm{h}}}$, [33],

$$Po = f Re_{D_{\mathrm{h}}}, \tag{33}$$

with

$$f = 8 \frac{\sigma^{\mathrm{w}}}{\rho_0 u^2} \quad \text{and} \quad Re_{D_{\mathrm{h}}} = \frac{\rho_0 u D_{\mathrm{h}}}{\mu_0}.$$

Here, u is the mean flow velocity,

$$u = \frac{1}{A} \int \int_A v_z \mathrm{d}A, \tag{34}$$

that in dimensionless form reads

$$\tilde{u} = \frac{u}{\sqrt{\theta_0}} = \frac{2}{\tilde{r}_{\mathrm{o}}^2 - \tilde{r}_{\mathrm{i}}^2} \int_{\tilde{r}_{\mathrm{i}}}^{\tilde{r}_{\mathrm{o}}} \tilde{v}_z \tilde{r} \mathrm{d}\tilde{r}. \tag{35}$$

Based on the dimensionless quantities and Eq. (32) the Poiseuille number depends on the Knudsen number as

$$Po = 2 \frac{|\wp|}{\tilde{u} Kn}. \tag{36}$$

Note that Knudsen number appears in the denominator of the above equation, and $\tilde{u}$ depends on the Knudsen number as well.

Fig. 6 depicts the Poiseuille number for a pipe ($\alpha = 0$) with fully diffusive walls ($\chi = 1$) and for a narrow annulus at $\alpha = 0.9$ with diffusive-reflective walls $\chi = 0.7$. For the case of pipe flow the well-known hydrodynamic relation $f Re_{D_{\mathrm{h}}} = 64$ is obtained in the limit $Kn \to 0$. The comparison to kinetic data [28] shows that NSF^2 and R13 provide satisfactory results for $Kn < 0.5$, while NSF^1 is accurate only for $Kn < 0.1$. For larger values of the Knudsen number NSF^1 overpredicts the Poiseuille number, but NSF^2 and R13 underestimate it. In particular this means that NSF^1 predicts a higher friction at large Knudsen numbers. It will be shown in the next section that due to the higher friction the NSF^1 model yields lower mass flow rate in highly rarefied situations.

Fig. 7 shows the trend for variation of the Poiseuille number with the annulus aspect ratio α, for $\chi = \{0.7, 1.0\}$. The annulus perimeter increases with α, so the friction increases, hence, larger Poiseuille numbers are observed for narrow annuli. However, kinetic data [28] show that this trend persists only until $Kn \approx 0.23$. For larger Knudsen numbers, the Poiseuille number decreases as α increases, but its drop is not significant. From the plots one can conclude that the proposed second-order slip condition (16) is efficacious to evaluate the Poiseuille number in this problem.

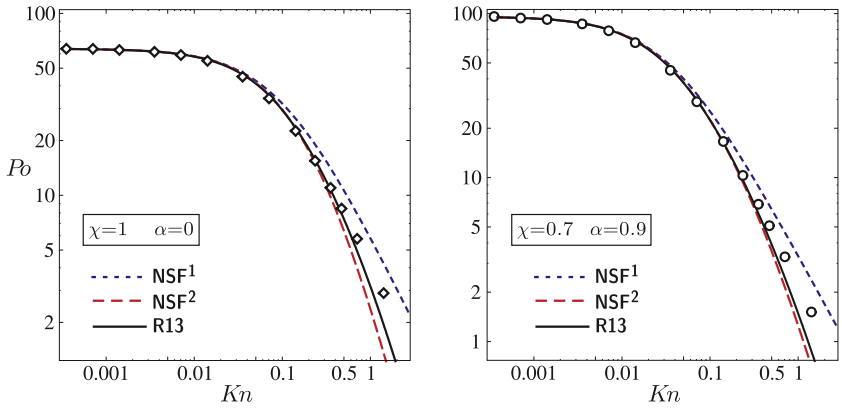

Fig. 6. Variation of Poiseuille number with respect to Knudsen number for NSF and R13 is compared to BGK kinetic data for a tube with fully diffusive walls (Left), and a narrow annulus with diffusive-reflective walls (Right). Diamonds and circles correspond to kinetic data from Ref. [28].

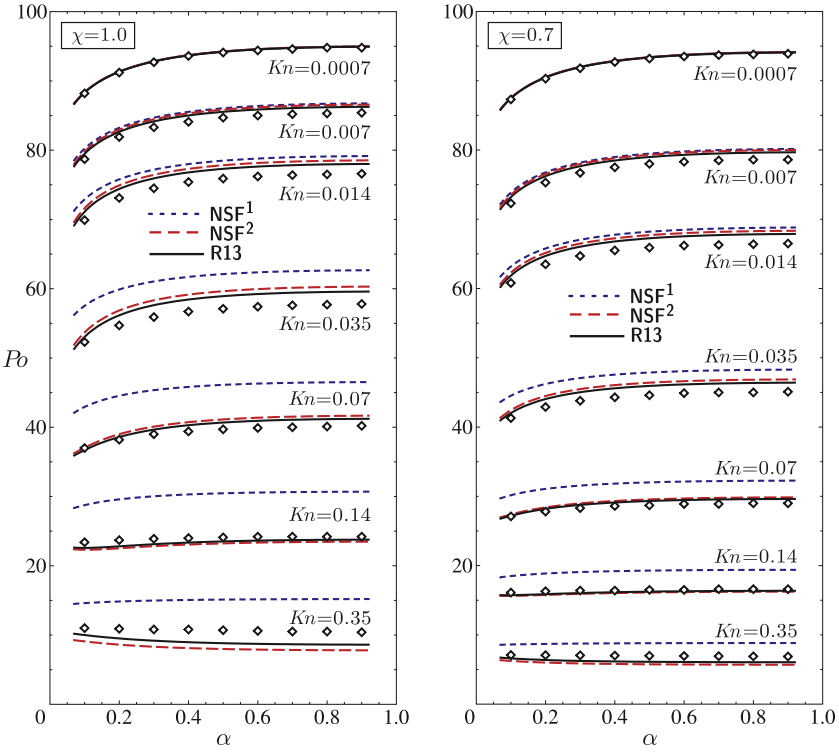

Fig. 7. Variation of Poiseuille number with respect to annulus aspect ration α is shown for fully diffusive walls (Left), and diffusive-reflective walls (Right). The R13 and NSF results for different Knudsen numbers are compared to BGK kinetic data for each case. Diamonds correspond to kinetic data from Ref. [28].

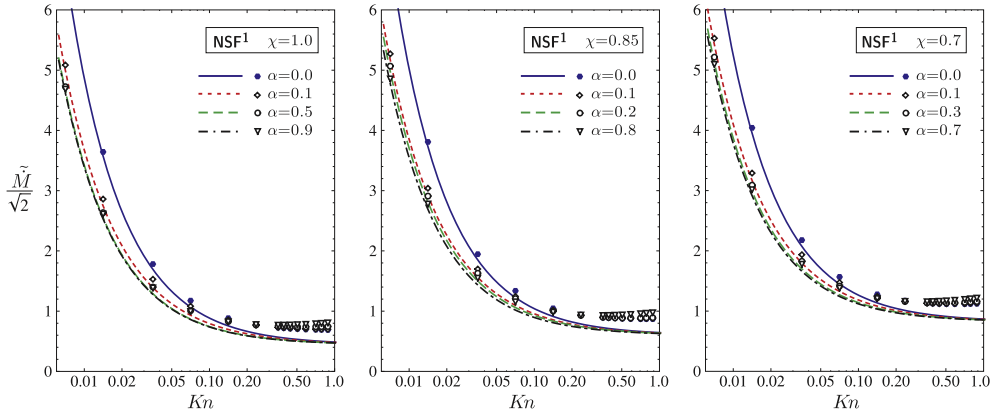

Fig. 8. Mass flow rate variations with respect to Knudsen number *Kn*, surface accommodation coefficient χ, and the ratio of inner to outer radius α, are compared between Navier–Stokes–Fourier with first-order slip condition and kinetic data. The BGK kinetic data from [28] are shown with different symbols for different annulus aspect ratios.

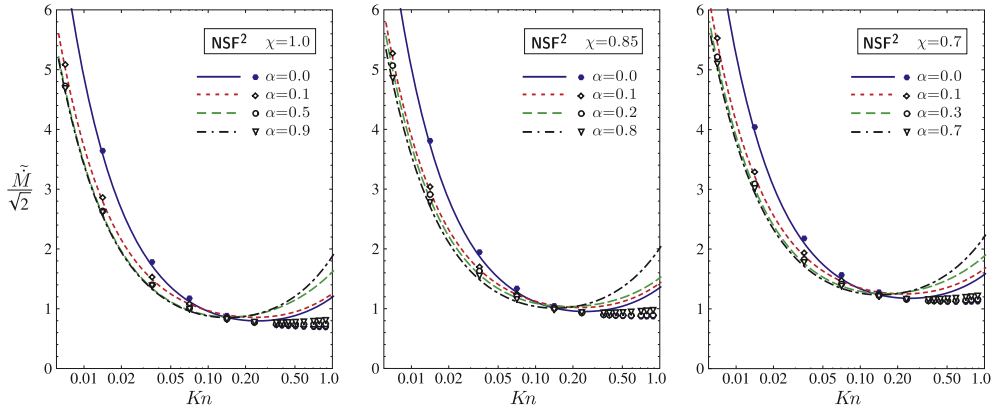

Fig. 9. Mass flow rate variations with respect to Knudsen number *Kn*, surface accommodation coefficient χ, and the ratio of inner to outer radius α, are compared between Navier–Stokes–Fourier with second-order slip condition and kinetic data. The BGK kinetic data from [28] are shown with different symbols for different annulus aspect ratios.

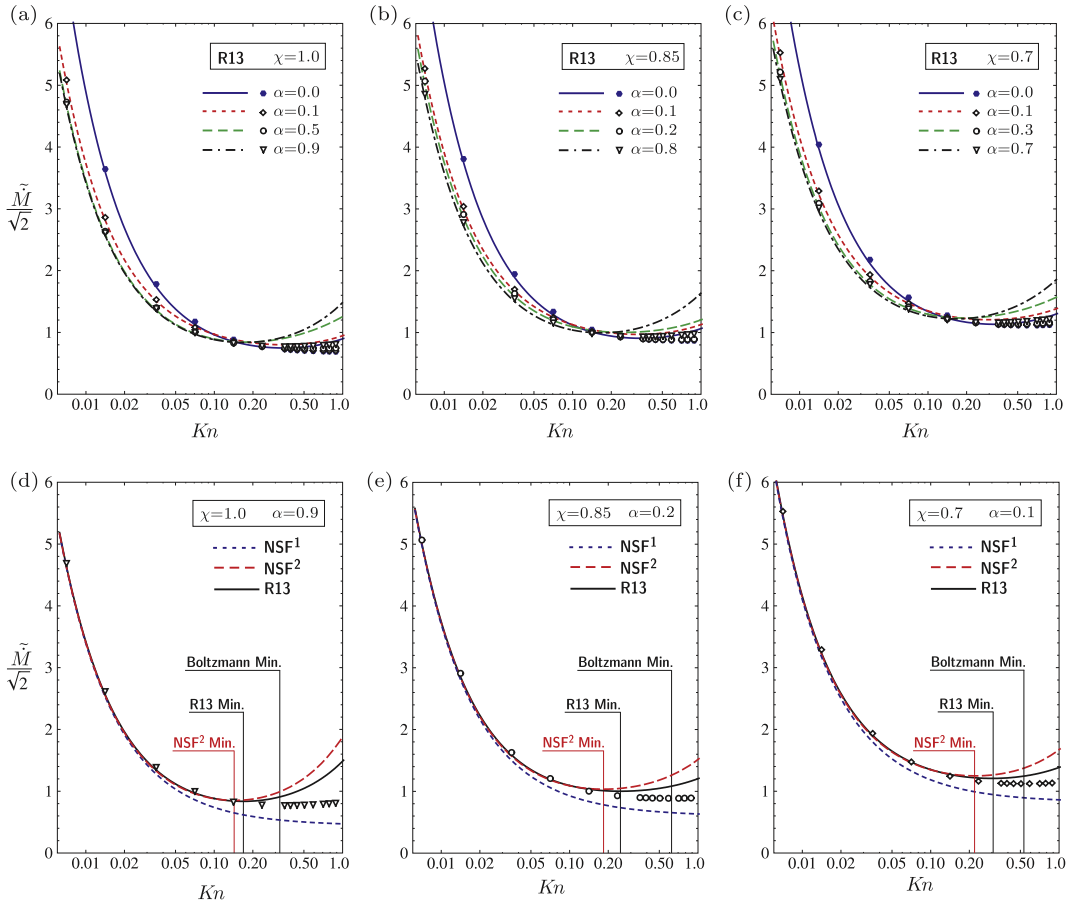

Fig. 10. (Plots (a)–(c)) Mass flow rate variations with respect to Knudsen number *Kn*, surface accommodation coefficient χ, and the ratio of inner to outer radius α, are compared between R13 and kinetic data. The BGK kinetic data from [28] are shown with different symbols for different annulus aspect ratios. (Plots (d)–(f)) Navier–Stokes–Fourier and R13 solutions for particular χ and α are compared to kinetic data [28].

6.2.2. Mass and thermal energy flow rates

Following the work of Lo et al. [27], isothermal mass and energy (thermal) flow rates in Poiseuille flow are given by phenomenological laws (for the linear case)

$$\dot{M} = \mathcal{F}\widetilde{\mathcal{M}} \quad \text{and} \quad \dot{E} = \theta_0 \mathcal{F}\widetilde{\mathcal{E}}, \tag{37}$$

where $\mathcal{F}$ is the thermodynamic force, and $\widetilde{\mathcal{M}}$ and $\widetilde{\mathcal{E}}$ are the dimensionless thermodynamic fluxes, respectively,

$$\mathcal{F} = -2\pi\ell^3 \frac{\rho_0\sqrt{\theta_0}}{p_0}\frac{\partial p}{\partial z}, \tag{38a}$$

$$\widetilde{\mathcal{M}} = \int_{\tilde{r}_i}^{\tilde{r}_o} \tilde{v}_z \tilde{r} \mathrm{d}\tilde{r}, \tag{38b}$$

$$\widetilde{\mathcal{E}} = \int_{\tilde{r}_i}^{\tilde{r}_o} \tilde{q}_z \tilde{r} \mathrm{d}\tilde{r}. \tag{38c}$$

In Ref. [28], where the hydraulic diameter is chosen as the reference length, $\ell = D_h = (A/\widetilde{A})^{1/2}$, the mass and energy flow rates in dimensionless form read

$$\widetilde{\dot{M}} = -\frac{2\dot{M}}{A\rho_0\sqrt{\theta_0}\wp} = \frac{4}{\check{r}_o^2 - \check{r}_i^2}\int_{\check{r}_i}^{\check{r}_o} \tilde{v}_z \check{r}\mathrm{d}\check{r}, \tag{39a}$$

$$\widetilde{\dot{E}} = -\frac{2\dot{E}}{Ap_0\sqrt{\theta_0}\wp} = \frac{4}{\check{r}_o^2 - \check{r}_i^2}\int_{\check{r}_i}^{\check{r}_o} \tilde{q}_z \check{r}\mathrm{d}\check{r}. \tag{39b}$$

Quite differently, in Ref. [27] the outer diameter is used as the reference length to evaluate the mass and energy flow rates, i.e., $\ell = r_o/\check{r}_o$, then

$$\widetilde{\dot{M}} = -\frac{2\dot{M}}{\pi r_o^2\rho_0\sqrt{\theta_0}\wp} = \frac{4}{\check{r}_o^3}\int_{\check{r}_i}^{\check{r}_o} \tilde{v}_z \check{r}\mathrm{d}\check{r}, \tag{40a}$$

$$\widetilde{\dot{E}} = -\frac{2\dot{E}}{\pi r_o^2 p_0\sqrt{\theta_0}\wp} = \frac{4}{\check{r}_o^3}\int_{\check{r}_i}^{\check{r}_o} \tilde{q}_z \check{r}\mathrm{d}\check{r}. \tag{40b}$$

In Figs. 8–10, variations of mass flow rate $\widetilde{\dot{M}}$, with respect to Knudsen number, surface accommodation coefficient χ, and the ratio of inner to outer radius of the annulus α, are shown. The symbols in the plots represent BGK kinetic data from Ref. [28]. In the kinetic simulations velocity is scaled as $\tilde{v}_z = v_z/\sqrt{2\theta_0}$, hence, $\widetilde{\dot{M}}/\sqrt{2}$ is plotted to match our results to the kinetic data.

The mass flow rate in the annulus increases when the accommodation coefficient χ decreases, since smaller values of χ represent smoother wall surfaces with less friction. The solution for a cylindrical tube is obtained for $\alpha \to 0$, while larger values for α correspond to narrower annuli. Kinetic solutions [28] confirm Knudsen's experimental observation [34,35], that in Poiseuille flow the mass flow rate as a function of Knudsen number exhibits a minimum around $Kn = 0.5$ (Knudsen minimum paradox).

Fig. 8 compares the NSF solution with first-order slip condition to the BGK data. The results show that this solution is valid only in the slip flow regime, $Kn \lesssim 0.05$. More importantly, it fails to predict any minimum in the mass flow rate.

Fig. 9 shows the NSF solution with second-order slip condition. Application of the second-order slip condition extends the validity of NSF equations to larger values of the Knudsen number, $Kn \lesssim 0.15$, and enables it to predict a minimum in the mass flow rates.

Plots (a)–(c) in Fig. 10 compare the R13 results with kinetic data. The R13 results give good agreement for $Kn \lesssim 0.3$, and also capture a minimum in the mass flow rate.

For better comparison, in plots (d)–(f) in Fig. 10, the macroscopic solutions are compared to kinetic data for some values of χ and α. Compared to the NSF solutions, improvments in the R13 results are due to the presence of Knudsen boundary layers in the velocity solution. Both NSF^2 and R13 overestimate the mass flow rate for large Knudsen numbers, because they predict larger slip (or less friction) than the Boltzmann equation.

In Fig. 11, NSF and R13 results for mass flow rate are compared to solutions of the linearized Boltzmann equation [27]. The comparisons are performed for fully diffusive walls, $\chi = 1$. For this comparison the coefficients in Eq. (11b) are used. Although the coefficients A and B are different for BGK and LB models, the discrepancy of LB data [27] with BGK data [28] is mainly due to the applied length scale, which is $D_h = 2\Delta r$ for the BGK case of Ref. [28] and $\Delta r = r_o - r_i$ for the LB case of Ref. [27].

In Fig. 12, the thermal energy flow rates obtained from the R13 equations are compared to kinetic data [27]. Results for both BGK

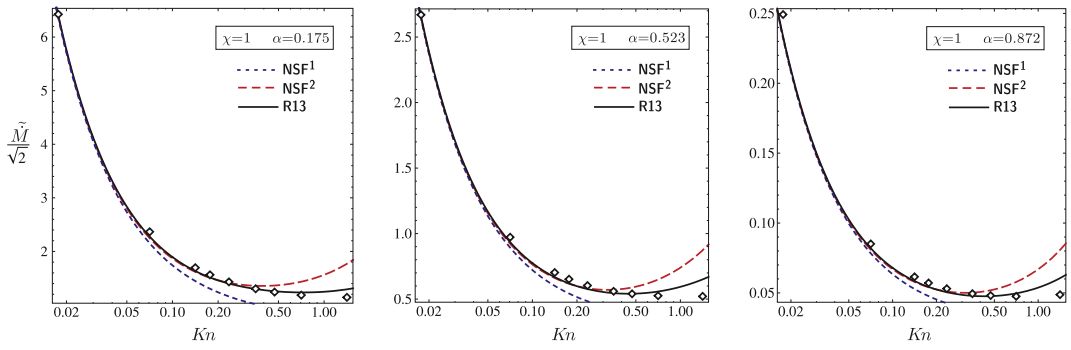

Fig. 11. Mass flow rate variations with respect to Knudsen number Kn, and the ratio of inner to outer radius α, for fully diffusive walls ($\chi = 1$) are compared between NSF, R13 and linear Boltzmann (LB) data [27].

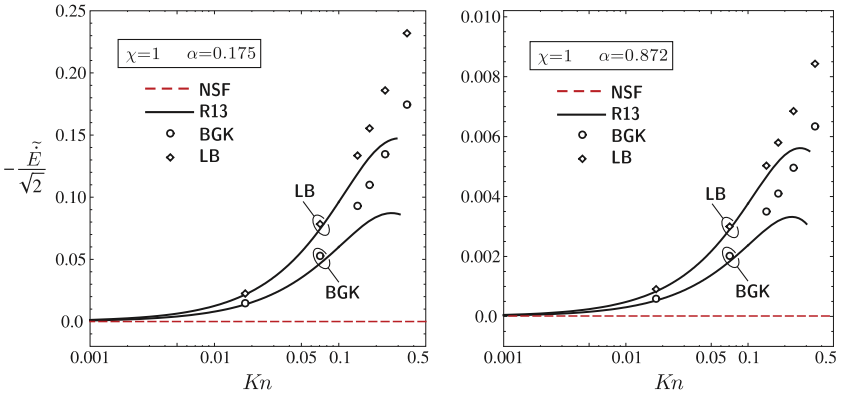

Fig. 12. Thermal energy flow rate variations with respect to Knudsen number Kn, and the ratio of inner to outer radius α, for fully diffusive walls ($\chi = 1$) are compared between NSF, R13 and kinetic data [27].

and LB models are depicted. Unlike the mass flow rate, which exhibits a minimum with respect to Knudsen number, the thermal energy flow rate always increases with Kn. The R13 results show acceptable accuracy for $Kn \lesssim 0.1$. This isothermal energy flow is absent in the NSF solution, $q_z^{\mathrm{NSF}} = 0$.

7. Conclusion

A compact analytical model based on the regularized 13-moment (R13) equations was employed to describe rarefied gas flows in tubes with annular cross section. Isothermal pressure-driven flows were investigated using linearized equations, where their solutions linearly depend on the driving force for the process, i.e., pressure gradient. The effects of gas rarefaction, annulus geometry, and surface accommodation on the solutions of shear stress, isothermal heat flux, and velocity were investigated.

Comparison of R13 solutions with kinetic solutions revealed that the dominant rarefaction effects in the considered flow are, (i) formation of Knudsen boundary layers, (ii) isothermal heat flux in the bulk flow, and (iii) slip velocity on the walls. The effects of these nonequilibrium phenomena on wall friction, mass flow rate, and thermal energy flow rates is thoroughly demonstrated, and compared to high-quality Boltzmann simulations. Our comparisons confirm that the R13 system successfully approximates kinetic solutions for $Kn < 0.5$ (of course, this range varies for different processes).

By comparing Navier–Stokes–Fourier (NSF) and R13 solutions, it is evident that the isothermal energy flow, which is triggered by Knudsen layers and a high-order bulk term, is absent in the NSF theory; this is where the real advantage of using R13 comes in. We highlighted the consequence of these NSF shortcomings in predictions of mass and energy flow rates, and showed that NSF are valid in the slip flow regime. However, application of second-order slip condition improves the NSF solution for higher ranges of Knudsen numbers.

A question may arise regarding how the solutions for the linearized R13 equations compare to numerical solutions of the full R13 equations? Numerical solution to nonlinear R13 equations for Couette and Poiseuille flows in parallel-plate channels are presented in [22], while for the same problems, linear and semilinear solutions are discussed in [14]. The nonlinear contributions lead to nonlinear high-order bulk effects as well as nonlinear contributions to the Knudsen layers (multiple Knudsen layers). As is discussed in particular in [14], these nonlinear effects are seen in kinetic solutions, and R13 reproduces them in good accuracy. However, these improvements are still limited to the early stages of the transition regime, where $Kn < 1$.

For the flow considered, second-order boundary conditions for NSF lead to quite good results for Poiseuille number and mass flow rate as long as the Knudsen number is sufficiently small. In this context it must be pointed out that even with second-order boundary conditions, NSF cannot predict rarefaction features like resolved Knudsen layers and non-Fourier heat flux. Due to the simple geometry of the present problem and the linearization, the thermal and mechanical problem of the flow are decoupled, and we have presented only the mechanical part: pressure, velocity, stress, and non-Fourier heat flux. For flows in more complex geometries thermal and mechanical problem cannot be decoupled; then, the non-Fourier heat flux will affect the temperature field, and similar effects from the thermal problem (e.g., non-Newtonian normal stresses) will affect the mechanical problem. Currently we are working on simulations of fully two-dimensional flows, where these coupling effects become visible in DSMC simulations and R13, showing flow details that cannot be reproduced with NSF.

To conclude, we point to the insufficiency of R13 equations for the description of highly rarefied flows ($Kn \simeq 1$), in which the magnitude of rarefaction effects is beyond the resolution of R13 equations. In such conditions, larger systems of moment equations [18] are suggested.

Acknowledgments

This research was supported by the Natural Sciences and Engineering Research Council (NSERC). P.T. gratefully acknowledges Dr. Majid Bahrami and his research group at the Laboratory for Alternative Energy Conversion (LAEC) at Simon Fraser University for their support.

References

[1] G.M. Karniadakis, A. Beskok, Micro Flows: Fundamentals and Simulation, Springer, New York, 2002.
[2] S. Chapman, T.G. Cowling, The Mathematical Theory of Non-uniform Gases, Cambridge University Press, Cambridge, 1970.
[3] C. Cercignani, Theory and Application of the Boltzmann Equation, Scottish Academic Press, Edinburgh, 1975.
[4] Y. Sone, Kinetic Theory and Fluid Dynamics, Birkhäuser, Boston, 2002.
[5] H. Struchtrup, Macroscopic Transport Equations for Rarefied Gas Flows, Springer, New York, 2005.
[6] H. Grad, On the kinetic theory of rarefied gases, Commun. Pure Appl. Math. 2 (1949) 325.
[7] H. Grad, Principles of the kinetic theory of gases, Handbuch der Phys., vol. 12, Springer, Berlin, 1958.
[8] H. Struchtrup, P. Taheri, Macroscopic transport models for rarefied gas flows: A brief review, IMA J. Appl. Math. 76 (2011) 672.
[9] H. Struchtrup, M. Torrilhon, Regularization of Grad's 13-moment equations: derivation and linear analysis, Phys. Fluids 15 (2003) 2668.
[10] H. Struchtrup, T. Thatcher, Bulk equations and Knudsen layers for the regularized 13 moment equations, Cont. Mech. Thermodyn. 19 (2007) 177.
[11] P. Taheri, A.S. Rana, H. Struchtrup, M. Torrilhon, Macroscopic description of steady and unsteady rarefaction effects in boundary value problems of gas dynamics, Cont. Mech. Thermodyn. 21 (2009) 423.
[12] X.-J. Gu, D. Emerson, G. Tang, Analysis of the slip coefficient and defect velocity in the Knudsen layer of a rarefied gas using the linearized moment equations, Phys. Rev. E 81 (2010) 016313.
[13] M. Torrilhon, H. Struchtrup, Regularized 13-moment-equations: shock structure calculations and comparison to Burnett models, J. Fluid Mech. 513 (2004) 171.
[14] P. Taheri, M. Torrilhon, H. Struchtrup, Couette and Poiseuille microflows: analytical solutions for regularized 13-moment equations, Phys. Fluids 21 (2009) 017102.
[15] H. Struchtrup, M. Torrilhon, Higher-order effects in rarefied channel flows, Phys. Rev. E 78 (2008) 046301.
[16] Y. Suzuki, S. Yamamoto, B. Leer, Q. Sun, I. Boyd, Application of the 10-moment model to mems flows, Comput. Fluid Dyn. 2004 (2006) 529.
[17] J.G. McDonald, C.P.T. Groth, Extended fluid-dynamic model for micron-scale flows based on Gaussian moment closure, in: AIAA Paper 2008-691, 46th AIAA Aerospace Meeting and Exhibit, 2008.
[18] X.-J. Gu, D.R. Emerson, A high-order moment approach for capturing non-equilibrium phenomena in the transition regime, J. Fluid Mech. 636 (2009) 177.
[19] A.V. Bobylev, The Chapman–Enskog and Grad methods for solving the Boltzmann equation, Sov. Phys. Dolk. 27 (1982) 29.
[20] H. Struchtrup, Stable transport equations for rarefied gases at high orders in the Knudsen number, Phys. Fluids 16 (2004) 3921.
[21] X.-J. Gu, D.R. Emerson, A computational strategy for the regularized 13 moment equations with enhanced wall-boundary conditions, J. Comput. Phys. 225 (2007) 263.
[22] M. Torrilhon, H. Struchtrup, Boundary conditions for regularized 13-moment-equations for micro-channel-flows, J. Comp. Phys. 227 (2008) 1982.
[23] P. Taheri, H. Struchtrup, Effects of rarefaction in microflows between coaxial cylinders, Phys. Rev. E 80 (2009) 066317.
[24] P. Taheri, H. Struchtrup, Rarefaction effects in thermally-driven microflows, Physica A 389 (2010) 3069.
[25] P. Taheri, H. Struchtrup, An extended macroscopic transport model for rarefied gas flows in long capillaries with circular cross section, Phys. Fluids 22 (2010) 112004.
[26] P. Bassanini, C. Cercignani, F. Sernagiotto, Flow of a rarefied gas in a tube of annular section, Phys. Fluids 9 (1966) 1174.
[27] S.S. Lo, S.K. Loyalka, T.S. Storvick, Rarefied gas flow in a cylindrical annulus, J. Vac. Sci. Technol. A 1 (1983) 1539.
[28] G. Breyiannis, S. Varoutis, D. Valougeorgis, Rarefied gas flow in concentric annular tube: estimation of the Poiseuille number and the exact hydraulic diameter, Eur. J. Mech. B Fluid 27 (2008) 609.

[29] F. Sharipov, V. Seleznev, Data on internal rarefied gas flows, J. Phys. Chem. Ref. Data 27 (1998) 657.
[30] P. Taheri, Macroscopic description of rarefied gas flow in the transition regime, Ph.D. thesis, University of Victoria, Victoria, BC, Canada, <http://www.dspace.library.uvic.ca:8080/handle/1828/3018?show=full> (2010).
[31] C. Maxwell, On stress in rarefied gases arising from inequalities of temperature, Phil. Trans. Roy. Soc. Lon. 170 (1879) 231.
[32] R.S. Myong, A full analytical solution for the force-driven compressible Poiseuille gas flow based on a nonlinear coupled constitutive relation, Phys. Fluids 23 (2011) 012002.
[33] F.M. White, Viscous Fluid Flow, McGraw-Hill, New York, 1991.
[34] M. Knudsen, Eine Revision der Gleichgewichtsbedingung der Gase. Thermische Molekularströmung, Ann. Phys. 31 (1910) 205.
[35] M. Knudsen, Thermischer Molekulardruck der Gase in Röhren, Ann. Phys. 33 (1910) 1435.